



## Reconstruction of concrete microstructure using complementarity of X-ray and neutron tomography

Hyeung-Tae Kim<sup>a</sup>, D. F. Tiana Razakamandimby R.<sup>a</sup>, Veronika Szilágyi<sup>b</sup>, Zoltán Kis<sup>b</sup>,  
László Szentmiklósi<sup>b</sup>, Michal A. Glinicki<sup>c</sup>, Youngsoo Park<sup>a,\*</sup>

<sup>a</sup> Department of Civil and Environmental Engineering, Yonsei University, 50 Yonsei-ro Seodaemun-gu, Seoul 120-749, Republic of Korea

<sup>b</sup> Nuclear Analysis and Radiography Department, Centre for Energy Research, H-1525 Budapest, P.O. Box 77, Hungary

<sup>c</sup> Institute of Fundamental Technological Research, Polish Academy of Sciences, Pawinskiego 5 B, 02-106 Warsaw, Poland

### ARTICLE INFO

#### Keywords:

Concrete microstructure  
X-ray tomography  
Neutron tomography  
Image segmentation  
Complementarity field  
Image-based analysis

### ABSTRACT

The concrete microstructure was successfully reconstructed using the complementarity of X-ray and neutron computed tomography (CT). Neither tomogram alone was found to be suitable to properly describe the microstructure of concrete under this study. However, by merging the information revealed by the two modalities, and using image segmentation, noise reduction, and image registration techniques we reconstruct the concrete microstructure. Void, aggregate, and cement paste phases are successfully captured down to the images' spatial resolution, even though the aggregate consists of multiple minerals. The coarse-aggregate volume fraction of the reconstructed microstructure was similar to that of the mixing proportions. Furthermore, image-based finite element analysis is performed to demonstrate the effects of microstructure on stress concentration and strain localization.

### 1. Introduction

The microstructure of concrete is an important characteristic in understanding material behavior, for example, under loads and environmental effects. The compositions, sizes, shapes, and arrangements of the various phases of distinct properties, present in concrete, constitute its microstructure. Owing to the inherent complexity and uncertainty of phase distinction, the description of the microstructure is challenging, and therefore various experimental and numerical approaches were developed to quantify microstructural features of concrete [1–3].

Recent advancements in visualization and volumetric imaging technologies made it possible to capture the concrete microstructure in 3D by employing X-ray and/or neutron computed tomography (CT). As X-ray attenuation coefficients mainly depend on the atomic number and the material density of the material, void spaces in concrete provide high contrast and therefore can be accurately identified. For example, X-ray CT images were used to investigate concrete microstructure associated with voids such as pore structure, microstructure-permeability relations, cracks under elevated temperature, self-healing process of concrete, and others (e.g., [4–12]). Unlike X-rays, the attenuation of a neutron beam is rather sensitive to the hydrogenous components. Then, neutron images

were used to investigate concrete shrinkage and durability concerning moisture movement (e.g., [13–19]). Further comprehensive reviews on X-ray and neutron tomography on cementitious material can be found in the literature [20,21].

Recently, a few studies have been performed using X-ray and neutron tomography and took advantage of the complementary nature of these two imaging modalities [22–29]. The use of the combined X-ray and neutron tomography in concrete science is very promising as the different X-ray and neutron attenuation coefficients result in different contrasts in the corresponding CT images. For example, the contrast between voids and solid in neutron image can be lower or even inverse than that in X-ray when voids are saturated with water/fluid [24] because neutrons are sensitive to hydrogenous components. Because the density of the cement paste might be similar to the density of aggregates, it is very challenging to identify aggregate and cement paste in an X-ray image alone. Then, a region-based segmentation technique was proposed to differentiate cement paste and aggregate in an X-ray CT image, where the chemical composition of aggregate was 97.3% of SiO<sub>2</sub> [30]. However, this was a simple mineral composition, that is insufficient to aid the analyses of polymineral aggregates. The deep learning technique was employed in the image segmentation of concrete microstructure

\* Corresponding author.

E-mail address: [k-park@yonsei.ac.kr](mailto:k-park@yonsei.ac.kr) (K. Park).

<https://doi.org/10.1016/j.cemconres.2021.106540>

Received 19 January 2021; Received in revised form 26 May 2021; Accepted 10 July 2021

Available online 28 July 2021

0008-8846/© 2021 The Author(s).

Published by Elsevier Ltd.

This is an open access article under the CC BY-NC-ND license

(<http://creativecommons.org/licenses/by-nc-nd/4.0/>).

[8,9,31], and the determination of the boundary between aggregates (i. e., quartz) and pastes was challenging [8,9]. To combine X-ray and neutron tomography, Tudisco et al. [32] and Roubin et al. [25] presented image registration techniques. Fedrigo et al. [22] published a comprehensive method to process bimodal images of a natural multi-phase system (meteorite) and segmentation of multiple mineral constituents. The use of bimodal images can provide an accurate representation of concrete microstructure especially when aggregate consists of multiple minerals.

The goal of this study was to reconstruct concrete microstructure with polymineral aggregates. A microstructure reconstruction process of concrete is presented using the complementarity of X-ray and neutron CT images in conjunction with image segmentation, noise reduction, and image registration techniques. Fine aggregate consists of fine quartz, while coarse aggregates are gabbro rock fragments containing more mineral phases. This composition results in various attenuation coefficients among aggregate clasts, and even inside gabbro rock fragments. Based on the presented image processing techniques, the reconstructed concrete microstructure is validated by comparing cumulative volume fractions. Additionally, the influence of reconstructed microstructure on the localized stress and strain fields in concrete is computationally demonstrated using a finite element simulation.

## 2. Image acquisition and preprocessing

Digital images were obtained using X-ray and neutron CT for a concrete specimen. Based on X-ray and neutron images, three material phases (void, paste, and aggregate) are preliminarily identified using a simple image segmentation technique. Scattering and signal noises in neutron CT images are reduced using filtering processes.

### 2.1. Specimen preparation and image acquisition

Concrete cube specimens (150 mm × 150 mm × 150 mm) were prepared using the mix design presented in Table 1. [33]. After nine months of moist curing, the specimen was cut to obtain a prismatic specimen with a size of 20 mm × 20 mm × 80 mm. The concrete mix design was intended for highly-trafficked highway pavement with exposed aggregates at the surface, to be exploited in a wet-freeze climate zone. Therefore, the mix was air-entrained to achieve the target air content of 5%, and aggregate gradation was selected appropriately for effective macrotexture of pavement [34]. Siliceous natural sand was used as fine aggregate, less than 2 mm in size. Crushed gabbro rock was used as a coarse aggregate fraction with the size of from 2 mm to 8 mm. The mineral composition of sand was mainly quartz. The thin-section analysis of gabbro aggregate grains revealed mainly plagioclases (labradorite-bytownite), metamorphosed amphiboles (hornblende), and rhombic pyroxene [35], as shown in Fig. 1.

Images of the specimen were obtained using X-ray and neutron CT. X-ray tomography images were taken at the Korea Institute of Civil Engineering and Building Technology using fan-beam projection. The distance between the source and specimen was 69.5 mm, and the distance between the detector and specimen was 916.5 mm with an image

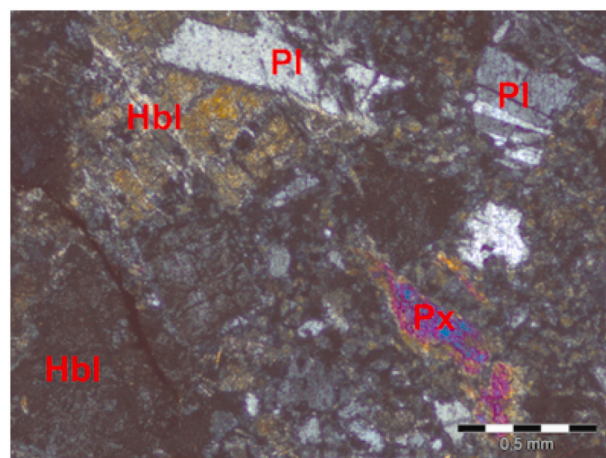


Fig. 1. Cross-section of gabbro grain with visible PI plagioclases, Hbl hornblende, and Px pyroxene (thin section, XPL, scale bar = 0.5 mm), source [35]

pixel size of 13.8  $\mu\text{m}$ . The thermal neutron tomography images were taken at the RAD facility of the Centre for Energy Research, Hungary [36] using cone-beam projection. The distance between the source and object was 4935 mm, and the distance between the detector and object was 35 mm with an image pixel size of 43.0  $\mu\text{m}$ . The real spatial resolution of the neutron CT images (taking into account the inherent, the geometrical and the reconstruction blurs) is around 235  $\mu\text{m}$ . Fig. 2(a) and (c) show 3D rendering of X-ray and neutron CT images for the concrete specimen, respectively; Fig. 2(b) and (d) illustrate the horizontal slice (20 mm × 20 mm) of X-ray and neutron CT images at the 14 mm height, respectively. The image sizes of the X-ray and neutron CT slices are 1500 × 1500 pixels and 510 × 510 pixels, respectively. In the first step of preprocessing, the originally 12 or 16-bit images were converted to 8-bit grayscale images (range of 0–255).

### 2.2. Image segmentation using Otsu-thresholding

A concrete specimen mainly consists of three phases such as void, paste, and aggregate. The gray intensity histogram of concrete CT images consists of three overlapping distributions corresponding to these materials, as schematically illustrated in Fig. 3. Nevertheless, three clear peaks were observed in the actual gray intensity histogram for the X-ray CT [Fig. 4(a)] and neutron CT [Fig. 5(a)]. Each peak region is denoted by “A”, “B”, and “C”.

In X-ray tomography, the gray intensity is mainly dependent on the average atomic number and the density of the material. For example, the lower gray intensity (darker pixels) corresponds to lighter material, as the air void in concrete, and thus the peak region of “A” is assigned to the void [see Fig. 4(a)]. Because the density of the aggregate is generally higher than that of the paste, the peak regions of “B” and “C” are the paste and the aggregate, respectively. For each 2D slice image, the thresholds ( $\theta_{X1}$ ,  $\theta_{X2}$ ) of multi-material phases are evaluated by the Otsu thresholding method with the Gaussian distribution [37]. Based on the computed thresholds, the regions of the void, paste, and aggregates are colored by yellow, light gray, and dark gray, respectively, as shown in Fig. 4(b). Additionally, because of local uncertainty of the data and material heterogeneity, gray intensity varies within each material phase (Fig. 3). Thus, gray intensities close to the thresholds may not provide accurate material phase separation, and those pixels are denoted as mixed-pixel. When the difference between the gray intensity ( $I_X$ ) and  $\theta_{X1}$  (or  $\theta_{X2}$ ) is equal or less than 3, the corresponding mixed-pixels are indicated as blue (or red), which are considered as the boundary regions between void and paste (or between paste and aggregate), as shown in Fig. 4(b). Furthermore, the density of some regions in aggregate is similar to cement paste density, and thus these two phases cannot be

Table 1

Concrete mixing proportions.

Mix component	Content (kg/m <sup>3</sup> Concrete mix)	Density (kg/m <sup>3</sup> )	Volume (dm <sup>3</sup> )	
Portland Cement	425	3.1	137.1	
Water	166	1	166.0	
Aggregate	Quartz 0–2 mm	525	198.1	
	Gabbro 2–8 mm	1267	448.0	
	Plasticizer	2.89	1.04	2.8
Admixture	Air entraining agent	0.77	1.05	0.7

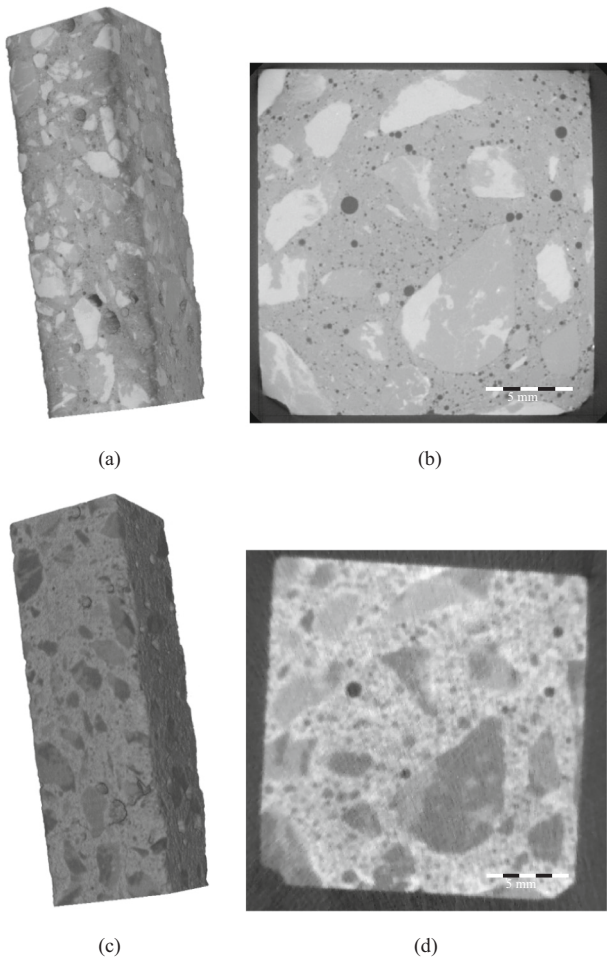


**Fig. 2.** (a) 3D rendering of X-ray CT image, (b) horizontal slice of X-ray CT image, (c) 3D rendering of neutron CT image, and (d) horizontal slice of neutron CT image for the concrete specimen with the size of 20 mm × 20 mm × 80 mm.

distinguished in certain regions if one only uses the gray intensity of X-ray CT image, [see Fig. 4(b)]. Unfortunately, if one manually shifts the threshold within the mixed-pixel regions, the complete aggregate region cannot be identified in this modality.

In neutron tomography, the neutrons are rather sensitive to hydrogenous components, and thus the resulting grayscale intensity contrast is different from the contrast of the X-ray CT image, as expected. For example, the gray intensity ( $I_N$ ) histogram of neutron tomography is illustrated in Fig. 5(a). Because of the relatively large amount of hydrogenous components in the cement paste, the gray intensity of cement pastes is higher than that of the aggregates, and thus the peak region of “C” belongs to cement paste. Voids providing the lowest gray intensity, just like in X-ray CT images, and they correspond to the peak region “A”. The peak region “B” corresponds to aggregates. Similarly, the thresholds ( $\theta_{N1}$ ,  $\theta_{N2}$ ) of multi-material phases are evaluated, and the segmented regions of the void, aggregate, and paste are shown in Fig. 5(b). Additionally, mixed-pixels associated with void-aggregate boundary are denoted by blue, i.e.,  $|I_N - \theta_{N1}| \leq 3$ , and mixed-pixels associated with aggregate-paste boundary are indicated by red, i.e.,  $|I_N - \theta_{N2}| \leq 3$ . Because of the lower spatial resolution in the neutron CT image, only relatively larger air voids are captured. However, relatively small aggregates (quartz) are well captured in the neutron CT images while they are not identified in the X-ray CT images. Some parts of coarse aggregates (gabbro) could be classified as cement paste with slightly adjusting the threshold within the mixed-pixel regions. Additionally, random small mixed-pixels in the aggregate and thin layer of aggregate are observed, which may be associated with signal and scattering noise and partial volume effects, as shown in red and blue boxes in Fig. 5(b), respectively. These noises are being reduced using filtering processes as explained in the following subsection.

2.3. Noise and sampling bias

In a neutron CT image, random small voids are observed within relatively large aggregates with the size of a few pixels when one uses the thresholds given by the Otsu method, as shown in Fig. 6(a). To remove the noise, the simple median filtering technique is used with a filter size of 3 by 3 pixels [38] instead of adjusting the thresholds. Fig. 6 (b) demonstrates that the noise within the aggregate is reduced.

Additionally, the image segmentation of the first attempt falsely identified a thin aggregate-like layer in-between void and cement paste

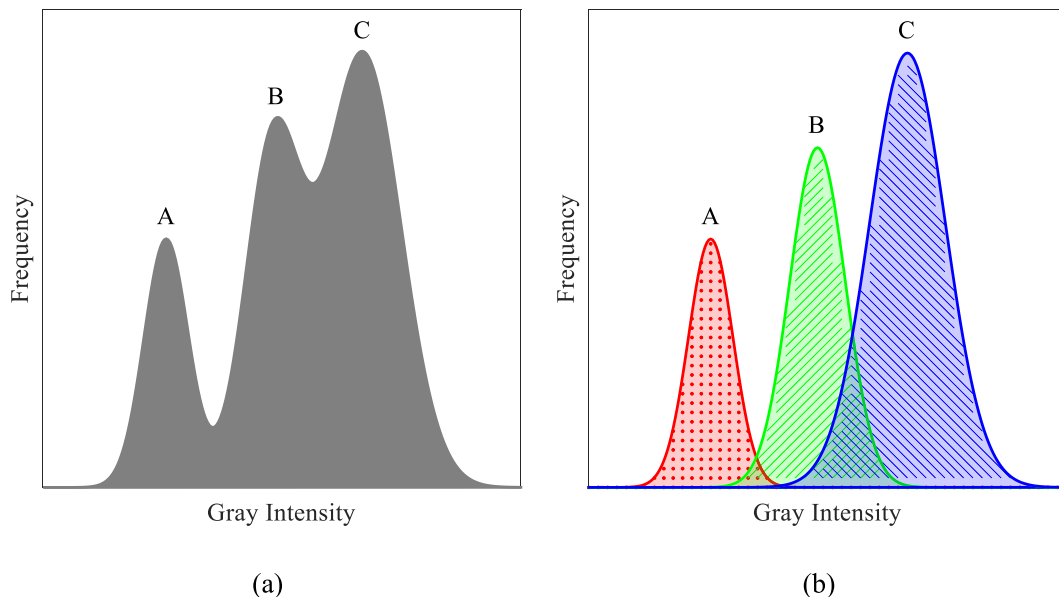


**Fig. 3.** (a) Schematic histogram of the gray intensity of CT image for a three-phase material, and (b) gray intensity histogram of each material phase.

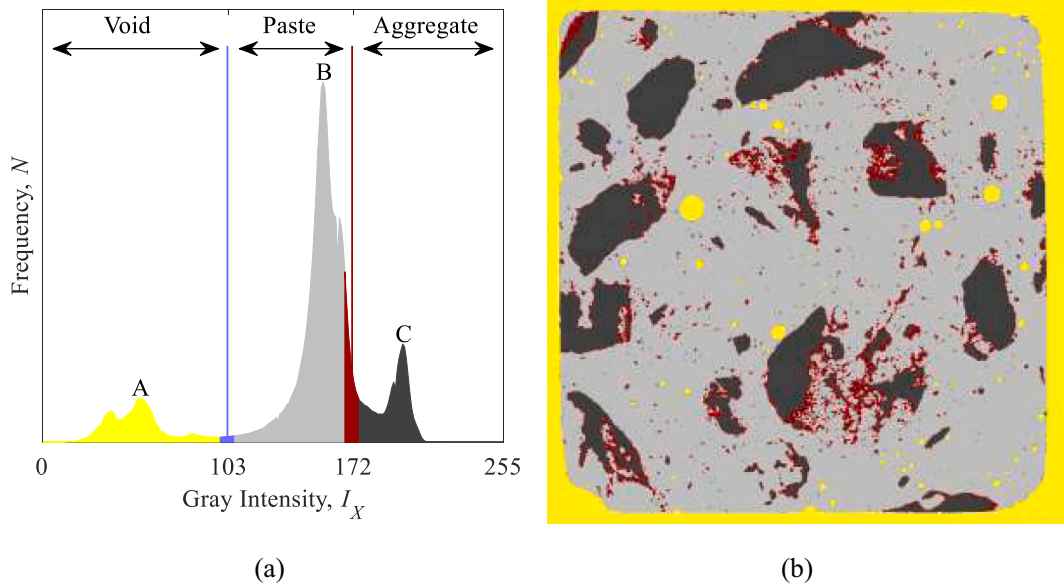


Fig. 4. (a) Gray intensity ( $I_X$ ) histogram of X-ray tomography, and (b) image segmentation result using the Otsu threshold.

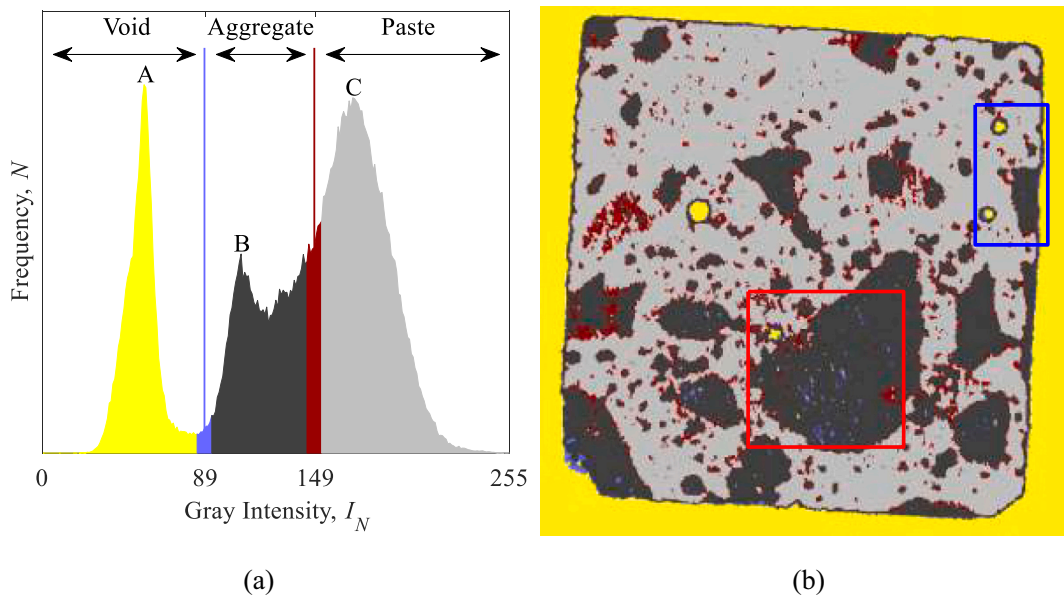


Fig. 5. (a) Gray intensity ( $I_N$ ) histogram of neutron tomography, and (b) image segmentation result using the Otsu threshold.

for neutron CT. One notes that the void region provides lower gray intensity, while the cement paste region demonstrates higher gray intensity; the aggregate region leads to intermediate gray intensity [see Fig. 5(a)]. Because of the partial volume effect (i.e. sampling biases of the gray intensity values near the edges) and, to some extent, from the elevated scattering noise in neutron tomography, the region at the boundary between air and paste results in an intermediate gray intensity between void and paste, whose value corresponds to the aggregate phase in this study. For example, the zoom of the original neutron CT image and the corresponding segmented image are shown in Fig. 7(a) and (b), respectively. The thin artificial aggregate layer region, identified using adjacent pixel information, is illustrated in green region in Fig. 7(c). To remove this artificial aggregate layer in the segmented neutron CT image, a modified threshold value ( $\bar{\theta}_N$ ) is used only for the segmentation of this artificial layer. The average of the multi-thresholds, i.e.,  $\bar{\theta}_N = (\theta_{N1} + \theta_{N2})/2$ , is used to segment the artificial layer into void and paste.

When the gray intensity is lower (or higher) than the average of the multi-thresholds, the corresponding pixel is considered as void (or paste), and the corresponding segmentation result is shown in Fig. 7(d).

Fig. 8(a) and (b) show the image segmentation results of X-ray and neutron tomography. Through the filtering process in the neutron CT image, the artificial thin layers along the boundary between void and paste phases are successfully rectified. However, it is very challenging to differentiate the three phases of the void, aggregate, and paste if one only uses the gray intensity of either the X-ray or the neutron CT image for the image segmentation. Although one could manually adjust thresholds with the mixed-pixel regions, the improvement on the segmentation result is limited, as discussed previously. Furthermore, because aggregate generally consists of multiple minerals, the image segmentation of X-ray and neutron CT images is in the practice even more challenging. It gave the importance of this study, which has achieved a microstructure reconstruction by making use of the

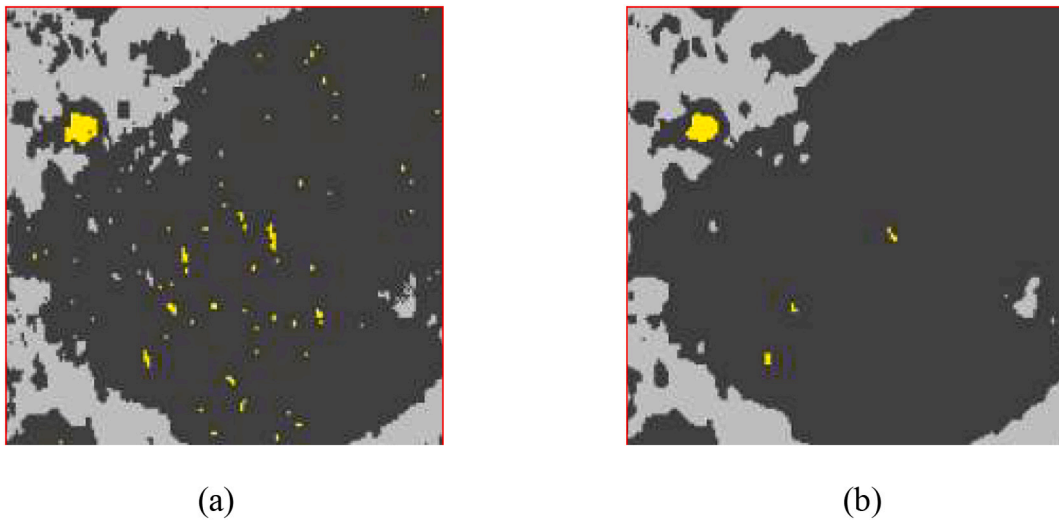


Fig. 6. Median filtering of neutron CT images: (a) original segmentation result using the Otsu threshold, and (b) segmentation result after using the median filtering.

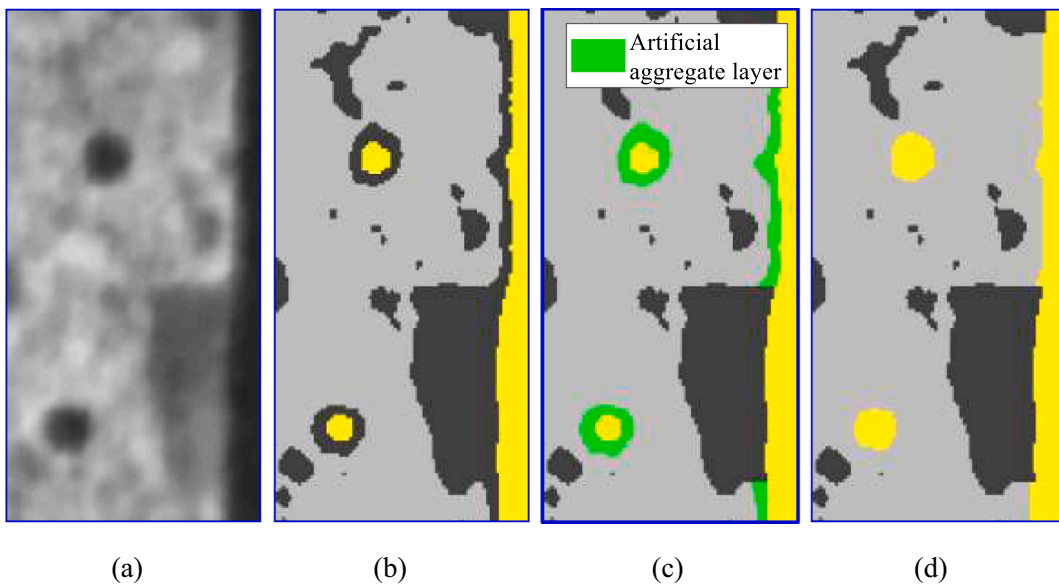


Fig. 7. Removing process of the artificial aggregate layers around void phase: (a) original neutron CT image, (b) original segmentation result using the Otsu threshold, (c) artificial aggregate layers (green pixels) between void phase and paste phase, and (d) segmentation result after removing the artificial layers. (For interpretation of the references to colour in this figure legend, the reader is referred to the web version of this article.)

complementarity of X-ray and neutron tomography.

### 3. Microstructure reconstruction with image registration

For the concrete microstructure reconstruction, X-ray and neutron CT images are combined using a feature-based image registration process. Because of the different spatial resolutions and orientations of the X-ray and the neutron CT volumetric datasets, the neutron CT images are scaled and aligned for each slice to match with the X-ray CT images. Then, the information contents of these two images are merged to reconstruct the concrete microstructure.

#### 3.1. Image registration

Because the image size of X-ray CT (13.8  $\mu\text{m}/\text{px}$ ) is larger than the size of neutron CT (43.0  $\mu\text{m}/\text{px}$ ), a neutron CT image is upscaled to have the same image size. The gray intensity ( $\bar{I}_N$ ) of the  $i$ -th row and  $j$ -th column pixel ( $\bar{p}_i, \bar{p}_j$ ) in the upscaled image corresponds to the gray

intensity ( $I_N$ ) of the original neutron image at the  $i$ -th row and  $j$ -th column pixel of ( $p_i, p_j$ ) where  $p_i$  and  $p_j$  are obtained by rounding up  $\alpha\bar{p}_i$  and  $\alpha\bar{p}_j$ , respectively, with the image size ratio ( $\alpha$ ) of X-ray CT to neutron CT ( $\alpha = 0.321$ ). Because both X-ray and neutron CT images are normal to the longitudinal direction of the specimen in this study, X-ray and neutron CT images are selected for the in-plane image registration at a given height. Then, the segmented neutron CT images are matched to the segmented X-ray CT image by rigid body translation and rotation within the plane. For example, the gray intensity of the X-ray CT image ( $I_X(x_X, y_X)$ ) at a point corresponds to the gray intensity of neutron CT image ( $\bar{I}_N(x_N, y_N)$ ). A given point ( $x_X, y_X$ ) in the X-ray CT image is mapped to a point ( $x_N, y_N$ ) in the neutron CT image, given as

$$\begin{bmatrix} x_N \\ y_N \end{bmatrix} = \begin{bmatrix} \cos\theta & \sin\theta \\ -\sin\theta & \cos\theta \end{bmatrix} \begin{bmatrix} x_X \\ y_X \end{bmatrix} + \begin{bmatrix} u_x \\ u_y \end{bmatrix} \quad (1)$$

where  $\theta$  is the rotation angle, and  $u_x$  and  $u_y$  are the horizontal and vertical translations. The magnitudes of the rigid body motion ( $\theta, u_x, u_y$ )

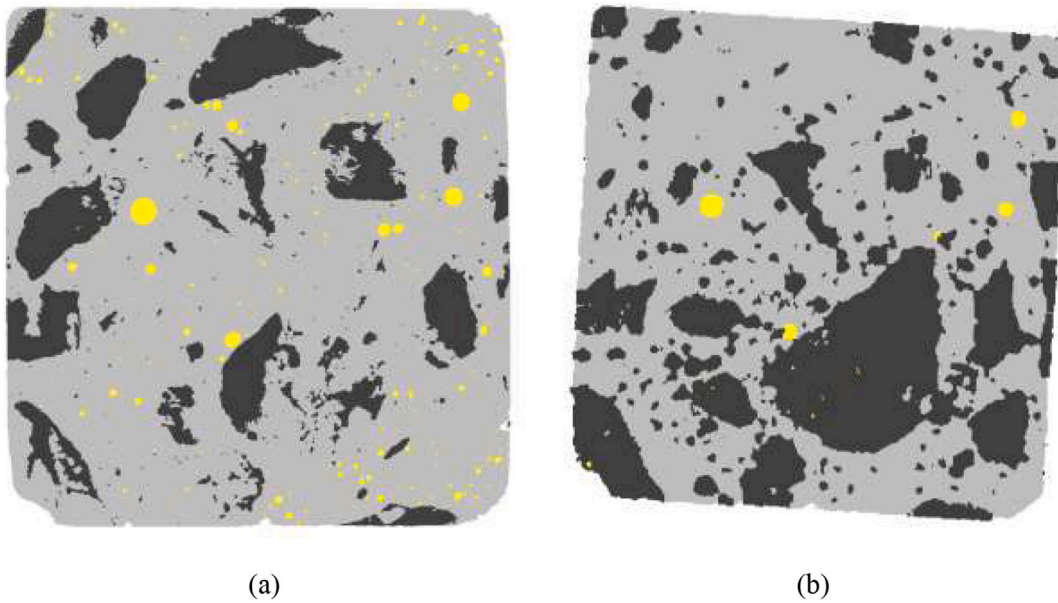


Fig. 8. Image segmentation results obtained from (a) X-ray CT image, and (b) neutron CT image after reducing noise and removing artificial aggregate layer.

are determined by minimizing the differences of reference (or feature) points, given as

$$\min_{\theta, u_x, u_y} \sum \left\| \begin{bmatrix} \cos\theta & \sin\theta \\ -\sin\theta & \cos\theta \end{bmatrix} \mathbf{P}_X^i + \begin{bmatrix} u_x \\ u_y \end{bmatrix} - \mathbf{P}_N^i \right\| \quad (2)$$

where  $\mathbf{P}_N^i$  and  $\mathbf{P}_X^i$  are the  $i^{\text{th}}$  reference points in the neutron and X-ray CT images, respectively. In this study, the reference points are selected as the centroids of the three largest voids in each image within the specimen domain for the alignment. The size of the void is determined by checking adjacent pixels of void pixels and assigning a unique index for each void.

Fig. 9 presents the combined X-ray and neutron CT images with the checkerboard pattern. The reference points are indicated as yellow cross markers. Within the 4 by 4 cells, the cells in either the odd row and even column or the even row and odd column are the image patches of X-ray

tomography; the cells in either the odd row and column or the even row and column are the image patches of neutron tomography. A good agreement is observed among adjacent image patches if one looks at the boundary between the aggregate and cement paste.

### 3.2. Microstructure reconstruction process

The concrete microstructure reconstruction process is explained in Algorithm 1. For a given height of the specimen, X-ray and neutron CT images are selected. Then, to reduce signal noise in neutron CT images, median filtering is employed. Next, the gray scale images are segmented using the Otsu threshold, and the artificial aggregate layer is rectified for the segmented neutron CT image. The segmented neutron CT image is scaled to match the pixel size of the segmented X-ray CT image. Then, they are aligned through considering rigid body rotation and translation, which completes the image segmentation and registration processes.

After the image segmentation and registration of the X-ray and neutron tomograms, material phases of the void, aggregate, and paste are determined by merging X-ray and neutron CT images with the following procedure. The set of void pixels ( $P_{\text{void}}$ ) is identified on the basis of the void pixels of the X-ray CT image ( $P_{\text{void},X}$ ), i.e.,  $P_{\text{void}} = P_{\text{void},X}$ , as it can identify the difference between void phase and solid phase with higher resolution and contrast, as discussed previously. For the determination of the aggregate pixel set ( $P_{\text{agg}}$ ), a potential aggregate region ( $\bar{P}_{\text{agg}}$ ) is defined first as the union of the aggregate pixel set of X-ray tomography ( $P_{\text{agg},X}$ ) and the aggregate pixel set of neutron tomography ( $P_{\text{agg},N}$ ), i.e.,  $\bar{P}_{\text{agg}} = P_{\text{agg},X} \cup P_{\text{agg},N}$  (this latter might contain voids as well). Then, the difference between the potential aggregate region ( $\bar{P}_{\text{agg}}$ ) and the set of void pixels ( $P_{\text{void}}$ ) is the set of aggregate pixel, i.e.,  $P_{\text{agg}} = \bar{P}_{\text{agg}} - P_{\text{void}}$ . Finally, the pixel set of paste is the complement of the void and aggregate sets. Based on the jointly evaluated X-ray and neutron CT images, Fig. 10(a), (b), and (c) illustrate the reconstructed concrete microstructure at vertical positions of 20 mm, 40 mm, and 60 mm, respectively, relative to the bottom of the specimen. The void, paste, and aggregate regions are colored in yellow, light gray, and dark gray, respectively. Additionally, the 3D concrete microstructure can be obtained from tacking 2D reconstructed concrete microstructure images. For example, 3D rendering of segmented concrete microstructures obtained from X-ray CT, neutron CT, and combined CT is illustrated in

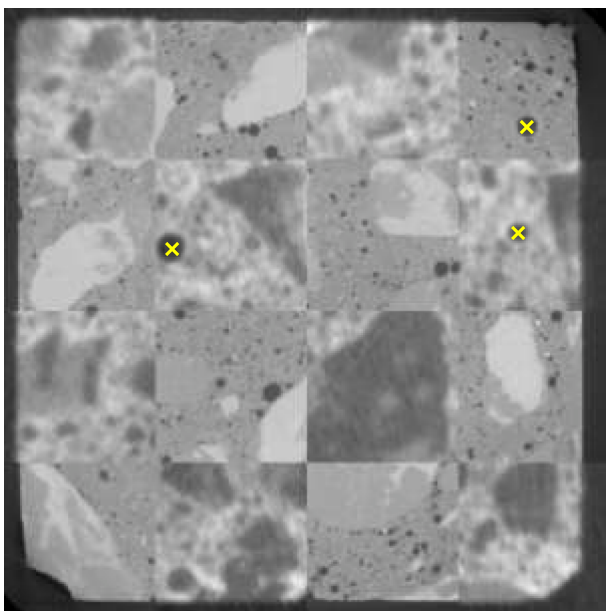


Fig. 9. Combined X-ray and neutron tomography with the checkerboard pattern.

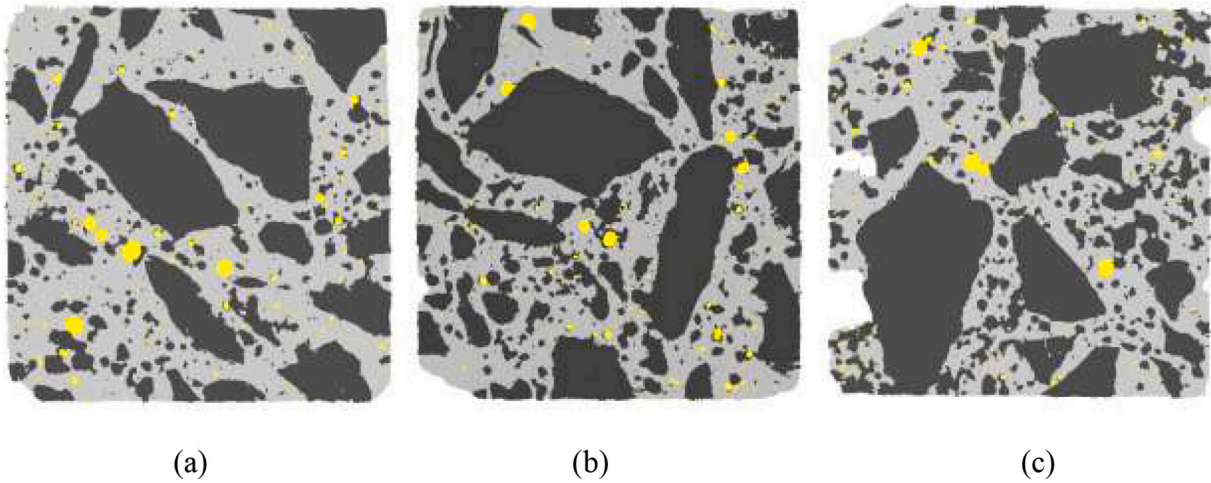


Fig. 10. Reconstructed concrete microstructure using the combined X-ray and neutron tomography at the sample height of (a) 20 mm, (b) 40 mm, and (c) 60 mm.

Fig. 11(a), (b), and (c), respectively. The domain size is 10 mm  $\times$  10 mm  $\times$  15 mm, and the aggregate and void phases are denoted by blue and yellow, respectively.

**Algorithm 1.** Process of concrete microstructure reconstruction.

1. Select X-ray and neutron CT images for a given height
2. Use the median filtering of neutron CT image to reduce signal noise
3. Segment the images using the Otsu method
4. Remove the artificial aggregate layer in the neutron segmented image
5. Scale the segmented images to match the pixel size
6. Register the segmented images within the transverse plane (rotation and translation)
7. Identify the material phases of void, aggregate, and paste

#### 4. Analysis of concrete microstructure

Based on the reconstructed concrete microstructure, the volume fraction of aggregates is computed to validate the presented image segmentation and registration process, and the aggregate phase is investigated using the two modalities of X-ray and neutron CT. Then, the finite element analysis is performed to demonstrate the effects of concrete microstructure on local stress and strain fields.

#### 4.1. Volume fraction

To validate the reconstructed microstructure using complementarity of X-ray and neutron tomography, the volume fraction of aggregate in the reconstructed microstructure is compared with the volume fraction in the concrete mixing proportions. The volume fraction of quartz and gabbro aggregates in the mixing proportion were 0.21 and 0.47, respectively. The size of quartz aggregate was less than 2 mm; while the size of gabbro aggregate was between 2 mm and 8 mm. Similarly, in the reconstructed concrete microstructure, aggregate is first classified based on its size. When the aggregate size is less (or greater) than 2 mm, the corresponding aggregate is shown in blue (or dark gray) to classify it as quartz (or gabbro), respectively [Fig. 12(a)]. In this study, the mean Feret diameter of each aggregate particle in a slice is assumed as the size of the corresponding (fine or coarse) aggregate. Fig. 12(b) demonstrates the cumulative volume fraction of constituent materials (coarse aggregate, fine aggregate, paste, and void) calculated separately for selected slices along with the specimen height. In this study, 31 cases are analyzed in between 10 mm and 70 mm with uniform spacing. The average volume fraction of larger aggregate is 0.43, which agrees well with the concrete mixing proportion. The average volume fraction of the fine aggregate, however, is just 0.077, which is considerably smaller than the fraction obtained from the mixing proportion. This is because of

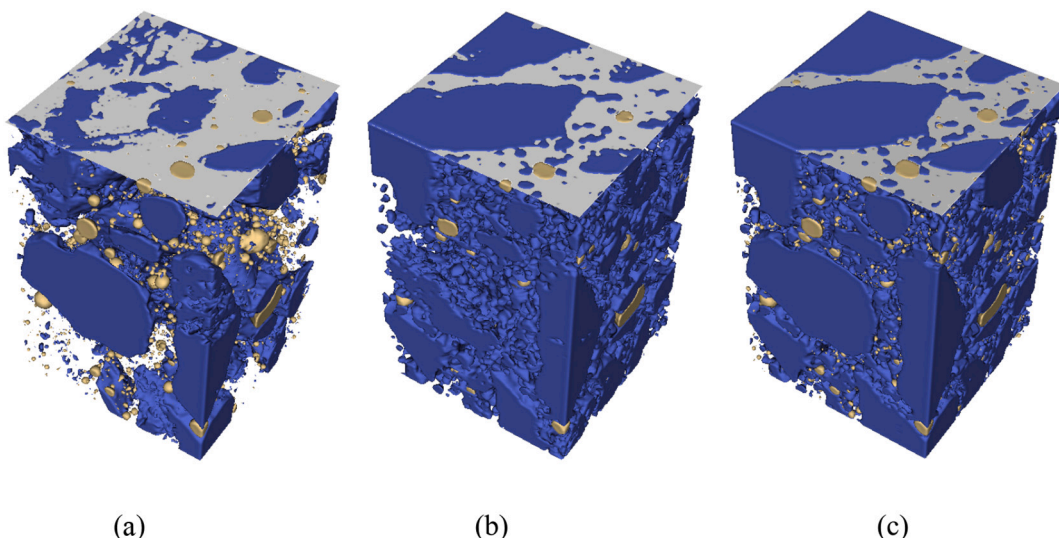
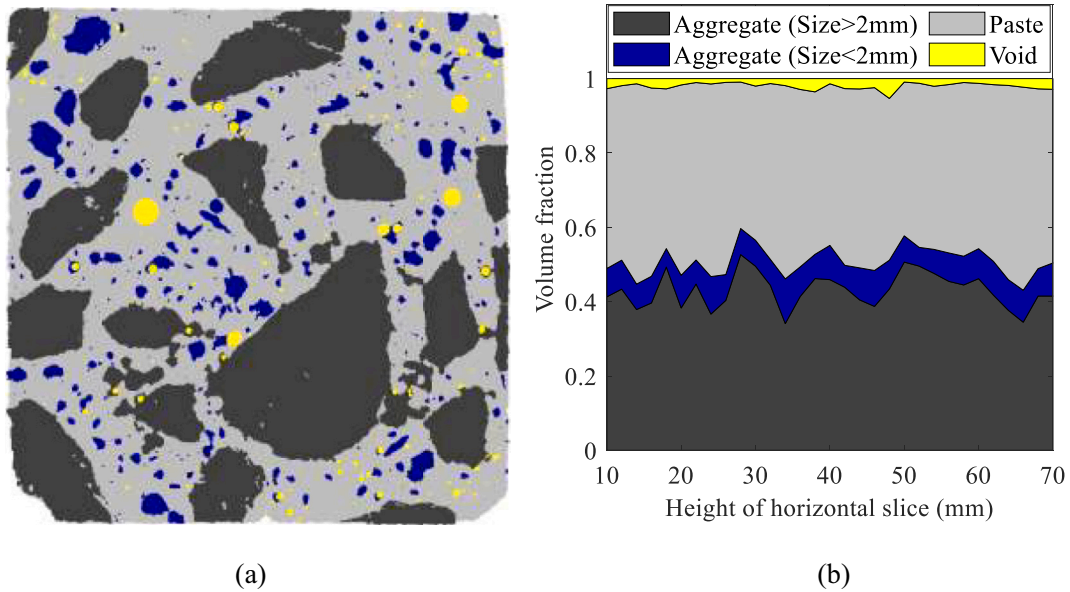


Fig. 11. Segmented aggregate and void phases obtained from (a) X-ray CT, (b) neutron CT, and (c) combined CT.



**Fig. 12.** (a) Concrete microstructure where aggregate size less (or greater) than 2 mm is in blue (or dark gray), and (b) the cumulative volume fraction of coarse aggregate, fine aggregate, paste, and void along with the specimen height. (For interpretation of the references to colour in this figure legend, the reader is referred to the web version of this article.)

the lower spatial resolution of neutron CT images. Although X-ray CT provided high resolution in this study, quartz was not differentiated from cement paste, as discussed previously. The void volume fraction of the reconstructed microstructure, 0.0204, is also lower than the volume fraction given by the mixing proportion, 0.0420, because the minimum void size captured in X-ray CT was approximately 30–40  $\mu\text{m}$  in this study, i.e. smaller voids were not detected.

Additionally, microstructure obtained from either X-ray or neutron tomography is shown in Fig. 13(a) and (b), respectively, for comparison. Then, the cumulative volume fractions of coarse aggregate, fine aggregate, paste, and void are computed using the three cases of microstructure, i.e., (1) microstructure from X-ray and neutron tomography (e.g., Fig. 12(a)), (2) microstructure from X-ray tomography (e.g., Fig. 13(a)), and (3) microstructure from neutron tomography (e.g.,

Fig. 13(b)). Then, the average cumulative volume fractions are compared with concrete mixing proportions (see Fig. 14). The comparison confirms that concrete microstructure using the combined X-ray and neutron tomography well reproduces coarse aggregate (gabbro) with multiple minerals.

#### 4.2. Aggregate phase

Because the aggregate phase is identified using the combined X-ray and neutron CT images, aggregate regions, and the corresponding gray intensities are shown in three colors according to the combination of segmentation results (see Fig. 15). The dark gray region is where both segmentation results of X-ray and neutron tomography are in the aggregate phase. The red (or green) region is where the segmentation of

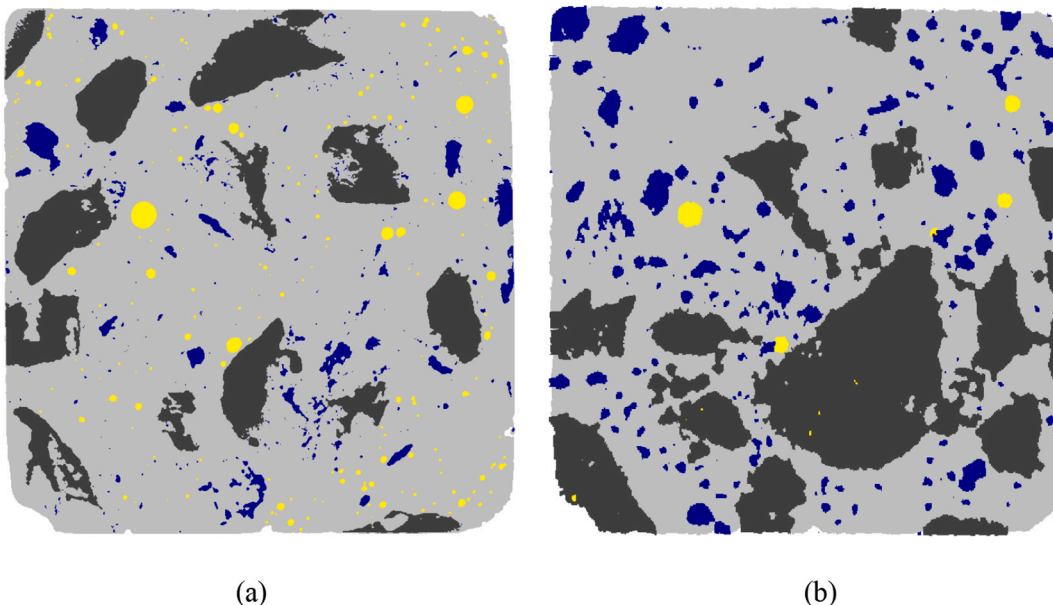


**Fig. 13.** Concrete microstructure obtained from the (a) X-ray CT image, and (b) neutron CT image.

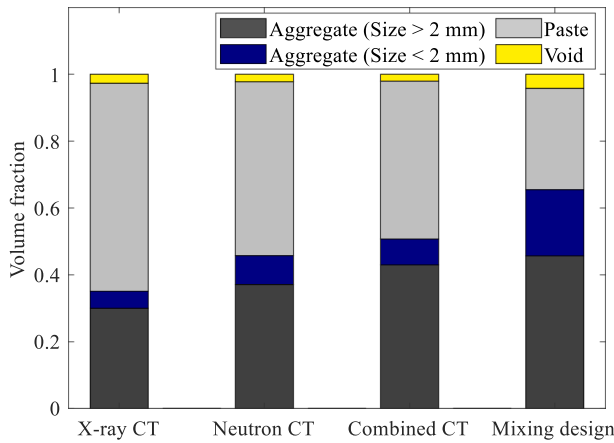


Fig. 14. Average cumulative volume fraction of coarse aggregate, fine aggregate, paste, and void obtained from X-ray CT, neutron CT, the combined X-ray and neutron CT, and mixing proportions.

X-ray (or neutron) CT images results in the aggregate phase, respectively. One notes that the relatively small-sized aggregates are mostly identified by neutron tomography, in spite it has a lower resolution. This is because the mineral of fine aggregates was generally quartz in this study. Concerning the X-ray modality, the density of quartz (2.648 g/cm<sup>3</sup>, [39]) is very similar to the density of C-S-H (2.604 g/cm<sup>3</sup>, [40]), thus no measurable contrast is expected. Concerning the neutron modality, the significant difference in the hydrogen content of quartz and C-S-H results in strong contrast. For relatively larger aggregates, only small

parts of coarse aggregate (dark gray regions in Fig. 15) are classified as aggregate by both X-ray and neutron CT images. The other parts of coarse aggregate (red and green regions in Fig. 15) are identified by either X-ray or neutron CT. This is because coarse aggregate is gabbro, which consists of multiple minerals; thus, the attenuation coefficient within coarse aggregate changes.

Because of the different mineral phases in aggregate, the segmentation is successful only by the combination of the results from the two modalities, as shown in Fig. 15. Identification of quartz (SiO<sub>2</sub>) and plagioclase feldspar (NaAlSi<sub>3</sub>O<sub>8</sub>-CaAl<sub>2</sub>Si<sub>2</sub>O<sub>8</sub>) is difficult by X-rays due to their similarly low densities to C-S-H paste. However, both quartz and plagioclase show low neutron attenuation values compared to C-S-H due to the hydrogen content of hydrated cement paste, which results in clear differentiation by neutron CT. Identification of higher density minerals, i.e. hornblende ((Ca,Na)<sub>2-3</sub>(Mg,Fe,Al)<sub>5</sub>(Al,Si)<sub>8</sub>O<sub>22</sub>(OH,F)<sub>2</sub>) and rhombic pyroxene ((Mg,Fe)<sub>2</sub>Si<sub>2</sub>O<sub>6</sub>) is successful by X-ray CT. However, due to its hydrogen content, hornblende has a neutron attenuation coefficient similar to the C-S-H paste, which makes the differentiation difficult. The bimodal aspect in imaging can help the segmentation of these and also similar common rock-forming minerals in the case of variable aggregate types of multi-phase composition.

#### 4.3. Finite element analysis of microstructure

Concrete with microstructure is analyzed using the finite element method. The three cases of concrete microstructure are employed: (1) microstructure using both X-ray and neutron CT images [e.g., Fig. 12 (a)], (2) microstructure using X-ray CT image [e.g., Fig. 13(a)], and (3) microstructure using neutron CT image [e.g., Fig. 13(b)]. Seven

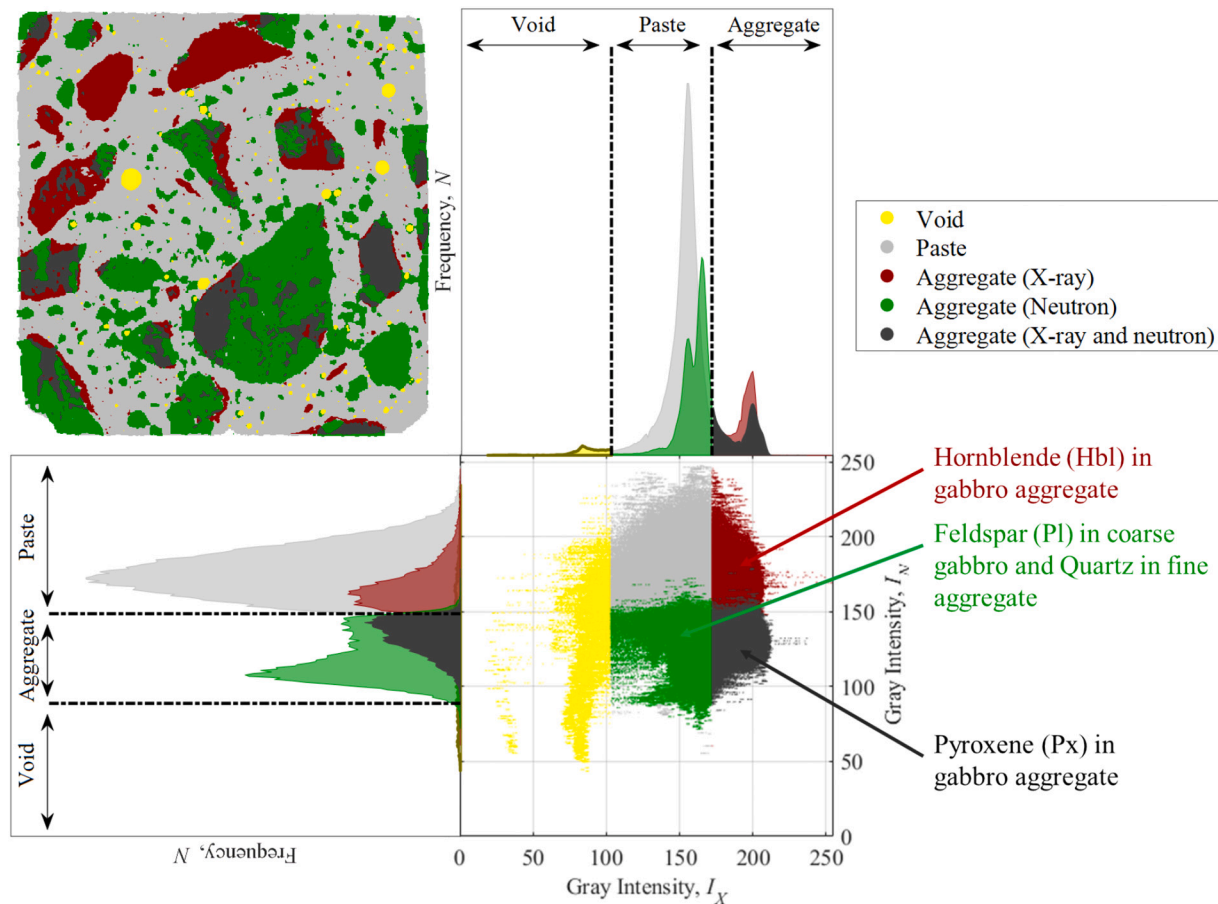


Fig. 15. Complementarity of X-ray and neutron tomography: (a) example of concrete microstructure, and (b) corresponding gray intensities of X-ray and neutron images.

horizontal slices of concrete microstructure are employed from 10 mm to 70 mm height; and additional microstructures are obtained through rotating them 90°, which leads to 14 concrete microstructures for each case. The microstructures are directly used for finite element analysis. A square domain of 18.5 × 18.5 mm (1340 × 1340 pixels) is selected, and each pixel corresponds to a four-node rectangular element. The uniaxial tensile displacement of 1.85 μm is applied along the vertical direction. A material type (i.e., aggregate or paste) is directly assigned to each element. For the void region, the corresponding elements (or pixels) are removed from the analysis because the stiffness of the void is zero. The numbers of nodes and elements are 1,775,539 and 1,781,355, respectively, when the void region is based on X-ray tomography. For the case of neutron tomography, the numbers of nodes and elements are 1,789,108 and 1,785,842, respectively. The elastic modulus and Poisson's ratio of aggregate are selected as 60 GPa and 0.25, respectively. For the cement paste, the elastic modulus is 20 GPa, and the Poisson's ratio is 0.2. The plane strain condition is assumed.

To investigate the effect of concrete microstructure on strain localization and stress concentration, the areas where the vertical strain is higher than 0.0002 and where the vertical stress is greater than 5 MPa are calculated for the three cases of 14 concrete microstructures. The corresponding area ratios to the total cross-section area are plotted in Fig. 16. The combined CT case generally provides a larger area of strain localization and stress concentration than the other two cases. The averaged area percentage of strain localization and stress concentration are summarized in Table 2 according to material phases for the combined CT, X-ray CT, and neutron CT cases. High strain localization is mostly observed in cement paste because aggregates provide higher stiffness than cement paste. For example, the computational results of the vertical stress and strain fields are illustrated in Figs. 17 and 18, respectively. The stress concentration is observed around voids. The strain on cement past is generally higher than that on aggregate because aggregates provide higher stiffness than cement paste, as expected. However, because of the different concrete microstructures, the computed local stress and strain are different from each other. For instance, the combined CT case provides relatively higher stress and strain in cement paste than the X-ray (or neutron) CT case, as illustrated in the box region of Figs. 17 and 18. This is because the combined CT case captures both voids and aggregates, while the X-ray (or neutron) CT case is limited to reconstruct the aggregate (or void) phase. Thus, computed local stress and strain are significantly affected by the local

**Table 2**

Average area percentage where the vertical strain is greater than 0.0002 (strain localization) and the vertical stress is higher than 5 MPa (stress concentration).

	Strain localization			Stress concentration		
	Aggregate	Paste	Total	Aggregate	Paste	Total
Combined CT	0.010	2.426	2.437	6.024	0.781	6.805
X-ray CT	0.000	0.842	0.842	0.841	0.323	1.165
Neutron CT	0.006	1.177	1.182	3.342	0.316	3.658

microstructure.

Additionally, the macroscopic material behavior also changes according to the microstructure. The computed elastic moduli are plotted in Fig. 19 for each concrete microstructure. The averaged elastic moduli are 32.4 GPa, 25.2 GPa, and 30.0 GPa for the combined, X-ray, and neutron CT cases, respectively. The elastic moduli are computed using the reaction forces on the displacement boundary. Because the aggregate volume fraction of the combined CT case is the highest, the resulting elastic modulus is also the highest in the analysis, as expected. In summary, the microstructure of concrete significantly affects material behaviors in both micro- and macro-scales.

**5. Conclusion**

For the investigation of concrete microstructure, the joint analysis and segmentation of X-ray and neutron tomography data are presented, and the complementary characteristics of their contrast mechanisms are utilized. Based on the gray intensities of each CT image, three phases of air void, aggregate, and paste are initially identified using image segmentation and noise reduction techniques. In neutron CT images, artificial aggregate-like layers are observed between the voids and the paste due to sampling bias and scattering noise, and these artifact layers are successfully eliminated. Based on feature-based image registration, X-ray and neutron CT images are fused, and concrete microstructure is successfully reconstructed, at least down to the image resolution.

The coarse aggregate volume fraction of concrete microstructure agrees well with that of the mixing design. However, if one only uses either X-ray or neutron tomography, the representation of concrete microstructure is limited because the coarse aggregate used in this study consists of multiple minerals. Additionally, fine aggregate is quartz, which provides very similar gray intensity with cement paste in X-ray

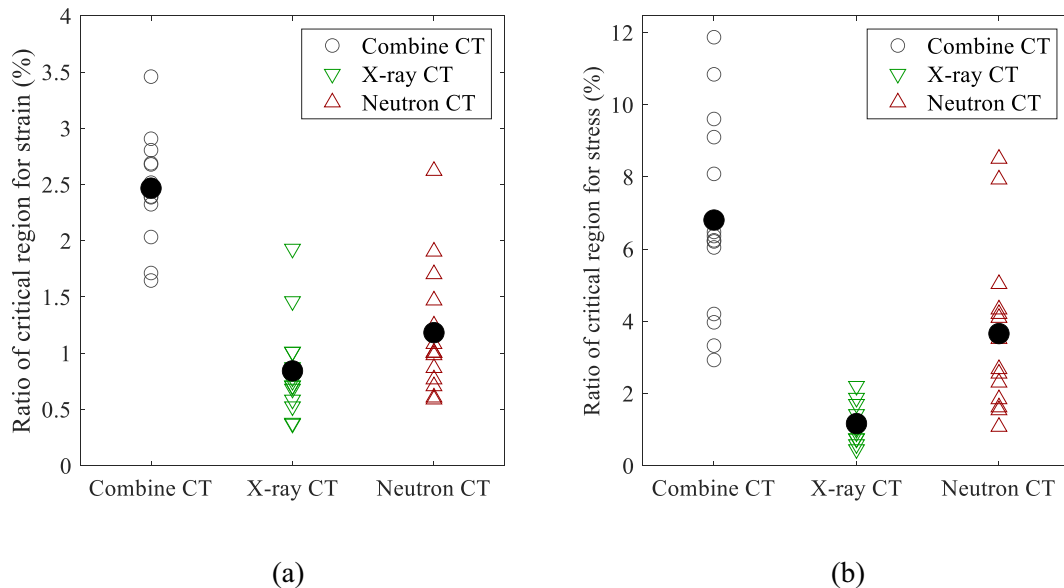


**Fig. 16.** Ratios of critical region associated with (a) strain localization, and (b) stress concentration.

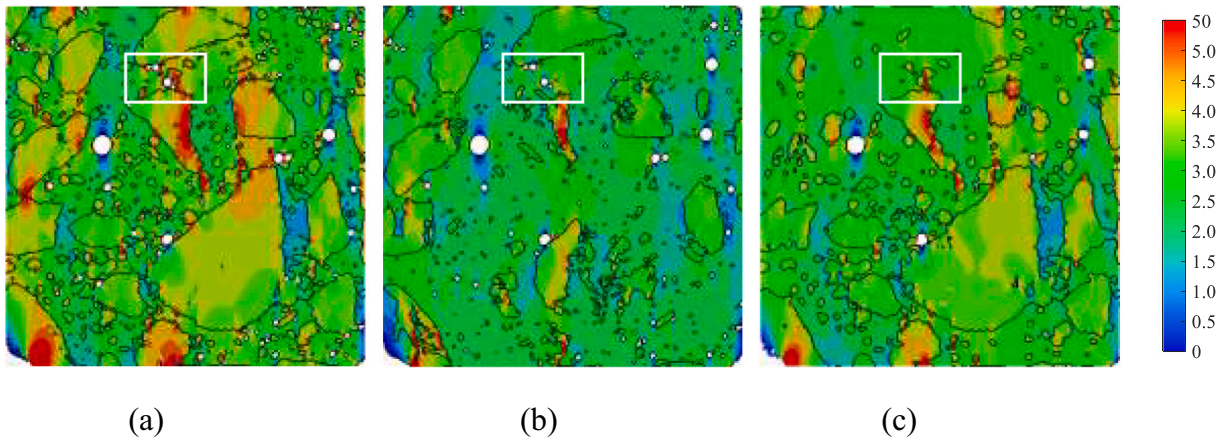


Fig. 17. Vertical stress field using the concrete microstructure obtained from the (a) combined X-ray and neutron CT, (b) X-ray CT, and (c) neutron CT under the uniaxial tension.

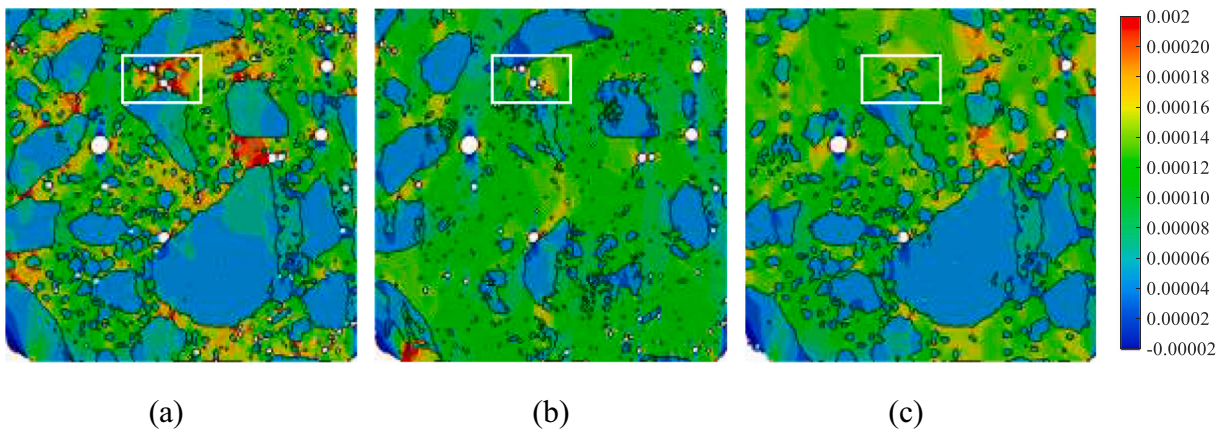


Fig. 18. Vertical strain field using the concrete microstructure obtained from the (a) combined X-ray and neutron CT, (b) X-ray CT, and (c) neutron CT under the uniaxial tension.

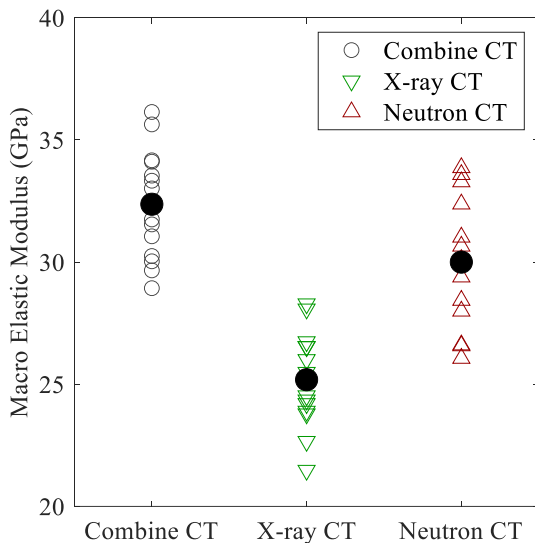


Fig. 19. Computational results of macroscopic elastic modulus.

tomography, and thus the fine aggregate is mostly identified based on the neutron tomogram in this study. Because of the large difference between the densities of the void phase and solid phase, voids are

identified using X-ray tomography, thanks to its high resolution and contrast. In neutron tomography, due to the lower spatial resolution of CT images, only relatively larger voids were observable. Furthermore, the effects of concrete microstructure on material behavior are demonstrated using finite element analysis. The microstructural differences revealed by the image reconstruction techniques significantly affect elastic modulus, stress concentration, and strain localization.

In summary, concrete microstructure obtained separately from either X-ray or neutron tomography may be of limited use for concrete that contains multiple minerals, if one just simply uses the gray intensity of one modality images for the image segmentation. Thus, further careful image processing techniques (e.g., the complementarity of X-ray and neutron tomography) should be employed for the accurate representation of 3D concrete microstructure.

**CRedit authorship contribution statement**

**Hyeung-Tae Kim:** Software, Methodology, Validation, Data curation, Formal analysis, Writing – original draft, Visualization. **D.F. Tiana Razakamandimby:** Software, Data curation, Formal analysis, Writing – review & editing, Visualization. **Veronika Szilágyi:** Data curation, Validation, Writing – review & editing. **Zoltán Kís:** Data curation, Writing – review & editing. **László Szentmiklósi:** Data curation, Writing – review & editing, Supervision, Project administration, Funding acquisition. **Michał A. Glinicki:** Data curation, Validation, Writing – review & editing, Supervision, Project administration, Funding

acquisition. **Kyoungsoo Park:** Conceptualization, Methodology, Writing – original draft, Supervision, Project administration, Funding acquisition.

### Declaration of competing interest

The authors declare that they have no known competing financial interests or personal relationships that could have appeared to influence the work reported in this paper.

### Acknowledgements

This work was supported by Visegrad Group (V4)-Korea Joint Research Program. HK, TR, and KP acknowledge the supports from the National Research Foundation of Korea funded by the Ministry of Science, ICT & Future Planning (grant number: 2017K1A3A1A67015884). The Hungarian co-authors acknowledge the project No. 127102 RADCON that has been implemented with the support provided from the National Research, Development and Innovation Fund of Hungary, financed under the NN\_17 V4-Korea funding scheme. The Polish co-author was supported by the Polish National Centre for Research and Development (Project V4-Korea/2/2018). The information presented in this paper represents the sole opinion of the authors and does not necessarily reflect the views of the sponsoring agencies.

### References

- [1] A.M. Brandt, *Cement-Based Composites: Materials, Mechanical Properties and Performance*, 2nd edition, CRC Press, 2009.
- [2] P.K. Mehta, P.J.M. Monteiro, *Concrete: Microstructures, Properties and Materials*, 4th ed., Prentice-Hall, New Jersey, USA, 2013.
- [3] H. Baek, C. Kweon, K. Park, Multiscale dynamic fracture analysis of composite materials using adaptive microstructure modeling, *International Journal for Numerical Methods in Engineering* 121 (2020) 5719–5741, <https://doi.org/10.1002/nme.6521>.
- [4] S.Y. Chung, J.S. Kim, D. Stephan, T.S. Han, Overview of the use of micro-computed tomography (micro-CT) to investigate the relation between the material characteristics and properties of cement-based materials, *Constr. Build. Mater.* 229 (2019) 116843.
- [5] V. Cnudde, A. Cwirzen, B. Masschaele, P.J.S. Jacobs, Porosity and microstructure characterization of building stones and concrete, *Eng. Geol.* 103 (2009) 76–83.
- [6] D. Fukuda, Y. Nara, Y. Kobayashi, M. Maruyama, M. Koketsu, D. Hayashi, H. Ogawa, K. Kaneko, Investigation of self-sealing in high-strength and ultra-low-permeability concrete in water using micro-focus X-ray CT, *Cem. Concr. Res.* 42 (11) (2012) 1494–1500.
- [7] K.Y. Kim, T.S. Yun, K.P. Park, Evaluation of pore structures and cracking in cement paste exposed to elevated temperatures by X-ray computed tomography, *Cem. Concr. Res.* 50 (2013) 34–40.
- [8] R. Lorenzoni, I. Curosu, F. Léonard, S. Paciornik, V. Mechtcherine, F.A. Silva, G. Bruno, Combined mechanical and 3D-microstructural analysis of strain-hardening cement-based composites (SHCC) by in-situ X-ray microtomography, *Cem. Concr. Res.* 136 (2020) 106139.
- [9] R. Lorenzoni, I. Curosu, S. Paciornik, V. Mechtcherine, M. Oppermann, F. Silva, Semantic segmentation of the micro-structure of strain-hardening cement-based composites (SHCC) by applying deep learning on micro-computed tomography scans, *Cem. Concr. Compos.* 108 (2020) 103551.
- [10] S. Lu, E.N. Landis, D.T. Keane, X-ray microtomographic studies of pore structure and permeability in Portland cement concrete, *Mater. Struct.* 39 (6) (2006) 611–620.
- [11] H.P. Pavani, T. Tadepalli, A.K. Agrawal, Estimation of porosity and pore distribution in hydrated Portland cement at elevated temperatures using synchrotron micro tomography, *J. Adv. Concr. Technol.* 17 (2019) 34–45.
- [12] R.D.F.T. Razakamandimby, K. Park, Characterization of air entrained concrete porosity using X-ray computed micro tomography image analysis, in: *Proceedings of the 12<sup>th</sup> International Symposium on Brittle Matrix Composites 2019*, BMC, 2019, pp. 139–146.
- [13] F.C. de Beer, W.J. Strydom, E.J. Griesel, The drying process of concrete: a neutron radiography study, *Appl. Radiat. Isot.* 61 (2004) 617–623.
- [14] D. Dauti, A. Tengattini, S. Dal Pont, N. Toropovs, M. Briffaut, B. Weber, Analysis of moisture migration in concrete at high temperature through in-situ neutron tomography, *Cem. Concr. Res.* 111 (June) (2018) 41–55.
- [15] C. Schroeel, V. Mechtcherine, P. Vontobel, J. Hovind, E. Lehmann, Sorption kinetics of superabsorbent polymers (SAPs) in fresh Portland cement-based pastes visualized and quantified by neutron radiography and correlated to the progress of cement hydration, *Cem. Concr. Res.* 75 (2015) 1–13.
- [16] P. Van den Heede, B. Van Belleghem, N. Alderete, K. Van Tittelboom, N. De Belie, Neutron radiography based visualization and profiling of water uptake in (un) cracked and autonomously healed cementitious materials, *Materials* 9 (2016) 311.
- [17] M. Wyrzykowski, P. Trtik, B. Münch, J. Weiss, P. Vontobel, P. Lura, Plastic shrinkage of mortars with shrinkage reducing admixture and lightweight aggregates studied by neutron tomography, *Cem. Concr. Res.* 73 (2015) 238–245.
- [18] K. Xu, A.S. Tremsin, J. Li, D.M. Ushizima, C.A. Davy, A. Bouterf, P.J.M. Monteiro, Microstructure and water absorption of ancient concrete from Pompeii: an integrated synchrotron microtomography and neutron radiography characterization, *Cem. Concr. Res.* 139 (2021) 106282.
- [19] M. Yehya, E. Andò, F. Dufour, A. Tengattini, Fluid-flow measurements in low permeability media with high pressure gradients using neutron imaging: application to concrete, in: *Nuclear Instruments and Methods in Physics Research, Section A: Accelerators, Spectrometers, Detectors and Associated Equipment* 890, 2018, pp. 35–42.
- [20] S. Brisard, M. Serdar, P.J.M. Monteiro, Multiscale X-ray tomography of cementitious materials: a review, *Cem. Concr. Res.* 128 (2020) 105824.
- [21] P. Zhang, F.H. Wittmann, P. Lura, H.S. Müller, S. Han, T. Zhao, Application of neutron imaging to investigate fundamental aspects of durability of cement-based materials: a review, *Cem. Concr. Res.* 108 (January) (2018) 152–166.
- [22] A. Fedrigo, K. Marstal, C. Bender Koch, V. Andersen Dahl, A. BJORHOLM DAHL, M. Lyksborg, C. Gundlach, F. Ott, M. Strobl, Investigation of a Monturaqui impactite by means of bi-modal X-ray and neutron tomography, *J. Imaging* 4 (2018) 72.
- [23] A. Kaestner, J. Hovind, P. Boillat, C. Muehlebach, C. Carminati, M. Zarebanadkouki, E.H. Lehmann, Bimodal imaging at ICON using neutrons and X-rays, *Phys. Procedia* 88 (2017) 314–321.
- [24] J.M. LaManna, D.S. Hussey, E. Baltic, D.L. Jacobson, Neutron and X-ray Tomography (NeXT) system for simultaneous, dual modality tomography, *Rev. Sci. Instrum.* 88 (11) (2017) 113702.
- [25] D. Mannes, F. Schmid, J. Frey, K. Schmidt-Ott, E. Lehmann, Combined neutron and X-ray imaging for non-invasive investigations of cultural heritage objects, *Phys. Procedia* 69 (2015) 653–660.
- [26] E. Roubin, E. Andò, S. Roux, The colours of concrete as seen by X-rays and neutrons, *Cem. Concr. Compos.* 104 (2019) 103336.
- [27] E. Stavropoulou, E. Andò, E. Roubin, N. Lenoir, A. Tengattini, M. Briffaut, P. Bésuella, Dynamics of water absorption in Callovo-Oxfordian claystone revealed with multimodal X-ray and neutron tomography, *Front. Earth Sci.* 9 (2020) 6.
- [28] A. Tengattini, N. Lenoir, E. Andò, B. Giroud, D. Atkins, J. Beaucour, G. Viggiani, NeXT-Grenoble, the neutron and X-ray tomograph in Grenoble, *Nucl. Inst. Methods Phys. Res. A* 968 (2020) 163939.
- [29] M. Wyrzykowski, S. Ghourchian, B. Münch, M. Griffa, A. Kaestner, P. Lura, Plastic shrinkage of mortars cured with a paraffin, based compound – bimodal neutron/X-ray tomography study, *Cem. Concr. Res.* 140 (2021) 106289.
- [30] O. Stamatii, E. Roubin, E. Andò, Y. Malecot, Phase segmentation of concrete X-ray tomographic images at meso-scale: validation with neutron tomography, *Cem. Concr. Compos.* 88 (2018) 8–16.
- [31] Y. Dong, C. Su, P. Qiao, L. Sun, Microstructural crack segmentation of three-dimensional concrete images based on deep convolutional neural networks, *Constr. Build. Mater.* 253 (2020) 119185.
- [32] E. Tudisco, C. Jailin, A. Mendoza, A. Tengattini, E. Andò, S. Hall, G. Viggiani, F. Hild, S. Roux, An extension of digital volume correlation for multimodality image registration, in: *Measurement and Technology* 28(9), IOP Publishing, 2017 (hal-01633737).
- [33] M. Dąbrowski, M.A. Glinicki, K. Dziedzic, A. Antolik, Validation of sequential pressure method for evaluation of the content of microvoids in air entrained concrete, *Constr. Build. Mater.* 227 (2019) 116633.
- [34] M. Dąbrowski, M.A. Glinicki, A. Gibas, A. Antolik, K. Dziedzic, Influence of surface retarders on texture profile and durability of upper layer of exposed aggregate concrete pavement, in: *Six International Conference on Durability of Concrete Structure 18–20 July 2018*. University of Leeds, Leeds, UK, 2018, p. PSE17.
- [35] D. Józwiak-Niedźwiedzka, A. Antolik, K. Dziedzic, M.A. Glinicki, K. Gibas, Resistance of selected aggregates from igneous rocks to alkali-silica reaction: verification, in: *Roads and Bridges-Drogi i Mosty* 18(1), 2019, pp. 67–83.
- [36] Z. Kis, L. Szentmiklósi, T. Belgya, M. Balaskó, L.Z. Horváth, B. Maróti, Neutron based imaging and element-mapping at the Budapest Neutron Centre, *Phys. Procedia* 69 (2015) 40–47.
- [37] N. Otsu, A threshold selection method from gray-level histograms, *IEEE Trans. Syst. Man Cybern.* 9 (1) (1979) 62–66.
- [38] T.S. Huang, G.J. Yang, G.Y. Tang, A fast two-dimensional median filtering algorithm, *IEEE Trans. Acoust. Speech Signal Process.* 27 (1) (1979) 13–18.
- [39] A. Smakula, V. Sils, Precision density determination of large single crystals by hydrostatic weighing, *Phys. Rev.* 99 (6) (1955) 1744–1746.
- [40] A.J. Allen, J.J. Thomas, H.M. Jennings, Composition and density of nanoscale calcium-silicate-hydrate in cement, *Nat. Mater.* 6 (4) (2007) 311–316.